Journal of Materials Chemistry C

ROYAL SOCIETY OF CHEMISTRY

PAPER

View Article Online
View Journal | View Issue

Cite this: J. Mater. Chem. C, 2022, 10, 16353

Exploring the influence of counterions on a hysteretic spin-transition in isomorphous iron(II) complex salts†‡

Thomas D. Roberts,[a] Christopher M. Pask,[a] Izar Capel Berdiell,[b] Floriana Tuna [c] and Malcolm A. Halcrow *[a]

$[FeL_2]X_2{\cdot}2H_2O$ (L = 2,6-bis{5-methyl-1*H*-pyrazol-3-yl}pyridine; X^- = BF_4^- or ClO_4^-) are readily dehydrated upon mild heating. Anhydrous $[FeL_2][BF_4]_2$ exhibits an abrupt spin-transition at $T_{1/2}$ = 205 K, with a 65 K thermal hysteresis loop which narrows upon repeated scanning. The isomorphous ClO_4^- salt remains high-spin on cooling, however, which is investigated further in this study. Unlike the iron complex, $[ZnL_2][ClO_4]_2{\cdot}2H_2O$ undergoes single-crystal-to-single-crystal dehydration; the tetragonal anhydrous crystals transform to a new triclinic phase upon cooling. The phase change is apparently sluggish and transition temperatures between 268 K and <200 K were measured by different techniques, implying it depends on the measurement conditions or sample history. Powder diffraction shows the zinc complex is a good model for the structural chemistry of $[FeL_2][ClO_4]_2$. The spin states of mixed-anion salts of the iron complex $[FeL_2][BF_4]_z[ClO_4]_{2-z}$ (z = 1.5 and 1.0) are also investigated. Their spin-transitions evolve more slowly on repeated scanning, as z decreases, and efficient thermally induced kinetic trapping is observed below 120 K when z = 1.0. Taken together, these data imply structural rearrangements in the anhydrous materials during thermal cycling occur more slowly in the presence of the larger ClO_4^- ion. Hence, rather than reflecting any structural differences with the SCO-active BF_4^- salt, the high-spin nature of $[FeL_2][ClO_4]_2$ is probably caused by kinetic inhibition of its putative spin-transition.

Received 30th August 2022,
Accepted 7th October 2022

DOI: 10.1039/d2tc03654a

rsc.li/materials-c

Introduction

The structural chemistry of cooperative, first order spin-crossover (SCO) transitions in solid materials is of continuing interest.[1–5] Materials applications of SCO compounds[5–9] as components in macroscopic devices[10–15] and in nano-electronics[16–18] are being continuously developed. Exploitation of those applications requires materials with bespoke switching properties, which usually (but not always) operate at room temperature. Producing new SCO materials to meet those specifications is still a challenging goal of molecular design and crystal engineering.[19–21] More fundamentally, SCO materials are useful mechanistic models of phase transitions in molecular crystals, at the macroscopic[22] and atomistic levels.[23,24]

SCO transitions exhibiting wide thermal hysteresis have particular interest.[25] Hysteretic spin-state switches are bistable at temperatures inside the hysteresis loop, which is a pre-requisite for applications requiring reversible switching at a specific temperature.[18,26,27] However, hysteresis is associated with large structural changes between the spin states,[28–36] which can lead to crystal decomposition during the transition.[37–40] The structural basis underpinning hysteretic SCO can thus be difficult to elucidate.[37–46]

We have reported that $[FeL_2]X_2{\cdot}2H_2O$ (Scheme 1; L = 2,6-bis{5-methyl-1*H*-pyrazol-3-yl}pyridine; **1a**·$2H_2O$, X^- = BF_4^-; **1b**·$2H_2O$, X^- = ClO_4^-) undergo facile and reversible dehydration on mild heating.[46,47] The anhydrous materials exhibit complex temperature-dependent structural chemistry on recooling by powder diffraction. For **1a**, this culminates in an abrupt spin-transition at $T_{1/2}$ = 205 K with a 65 K thermal hysteresis loop (although the hysteresis gradually narrows when the transition is cycled multiple times).[46] In contrast, anhydrous **1b** remains

[a] School of Chemistry, University of Leeds, Woodhouse Lane, Leeds, LS2 9JT, UK. E-mail: m.a.halcrow@leeds.ac.uk
[b] Center for Material Science and Nanomaterials (SMN), University of Oslo, Sem Sælands 26, 0371 Oslo, Norway
[c] School of Chemistry and Photon Science Institute, University of Manchester, Oxford Road, Manchester, M13 9PL, UK

† Data supporting this study are available at DOI: https://doi.org/10.5518/1233

‡ Electronic supplementary information (ESI) available: Previously published magnetic susceptibility data for the **1a**·$2H_2O$ and **1b**·$2H_2O$, illustrating their different spin state behaviours; crystallographic data, refinement details, figures and tables; and other solid state characterisation data for the new materials in this study. CCDC 2195223–2195228. For ESI and crystallographic data in CIF or other electronic format see DOI: https://doi.org/10.1039/d2tc03654a

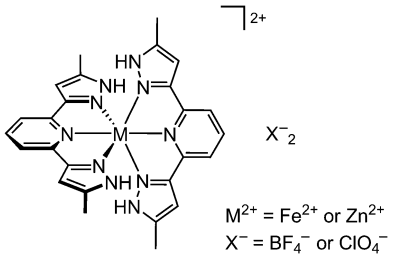

Scheme 1 Structures of $[FeL_2]X_2$ (**1a**, X^- = BF_4^-; **1b**, X^- = ClO_4^-) and $[ZnL_2]X_2$ (**2a**, X = BF_4^-; **2b**, X^- = ClO_4^-).

high-spin at all temperatures, despite being isomorphous with the BF_4^- salt by powder diffraction (Fig. S1, ESI‡).[47]

The structural basis for these behaviors could not be probed crystallographically, because the crystals of **1a**·$2H_2O$ and **1b**·$2H_2O$ decompose during the dehydration reaction. However a more recent study of $[ZnL_2][BF_4]_2$·$2H_2O$ (**2a**·$2H_2O$), whose crystals survive the dehydration process, shed some light on the question.[48] Dehydrated crystals of **2a** (phase B; tetragonal, $P4_2/n$, $Z = 2$) are isomorphous with anhydrous **1a** by powder diffraction. The anhydrous zinc crystal undergoes a phase transition near room temperature to triclinic phase C ($P\bar{1}$, $Z = 2$). Unexpectedly, the structure of phase C evolves continuously on further cooling. That reflects a temperature-dependent molecular structure distortion of the complex cation, involving a rotational displacement of one L ligand around the metal ion as the temperature is lowered. The same temperature dependence is also shown by phase C of **1a**, by powder diffraction. The spin-transition in **1a** involves a transformation from phase C to a new low-spin phase (phase E), which was not structurally characterised but may involve a tripling of the phase C asymmetric unit.[48]

We now report further investigations of the different behavior of **1a** and **1b**, through two experiments. First is a structural investigation of $[ZnL_2][ClO_4]_2$ (**2b**), as a model for the high-spin iron perchlorate salt **1b**. Second, is a series of mixed-anion formulations $[FeL_2][BF_4]_z[ClO_4]_{2-z}$, to probe how SCO in **1a** evolves as the anion composition changes in the material.[49–51]

Results and discussion

As per our previous study,[48] **2b** was synthesised by treatment of hydrated $Zn[ClO_4]_2$ with 2 equiv. L in methanol, which yielded a white microcrystalline solid after the usual work-up. In contrast to the BF_4^- salt **2a**, **2b** is too insoluble in water to be recrystallised from that solvent. However, slow recrystallisation from undried nitromethane using diethyl ether vapour as antisolvent yielded small pale yellow crystals of the hydrate phase **2b**·$2H_2O$. Six datasets were collected and refined from one of these crystals, under the conditions described below.

The structural chemistry of **2b**·$2H_2O$ resembles **2a**·$2H_2O$.[48] The as-isolated crystal adopts the tetragonal space group $P4_2/n$ with $Z = 2$. A unique one-quarter of a complex molecule lies on a $\bar{4}$ symmetry site, with half-ClO_4^- and half-water equivalents being disordered within the same lattice cavity near a crystallographic C_2 axis. The lattice is a form of ''terpyridine embrace'',[52] with four-fold interdigitated cation layers in the (001) plane which are separated by hydrogen bonded chains of anions and water molecules (Fig. 1, left). Each pyrazolyl group in the complex forms N–H···O hydrogen bond to two anions and two water molecules, in a random distribution reflecting the local four-fold crystallographic symmetry.

In situ dehydration of the **2b**·$2H_2O$ crystal was achieved by annealing at 350 K on the diffractometer for 30 minutes. The anhydrous crystal exhibits the same crystal symmetry between 350–200 K (tetragonal, $P4_2/n$, $Z = 2$; phase B). Data from phase B were collected at four temperatures within that range, and showed minimal differences in each case.

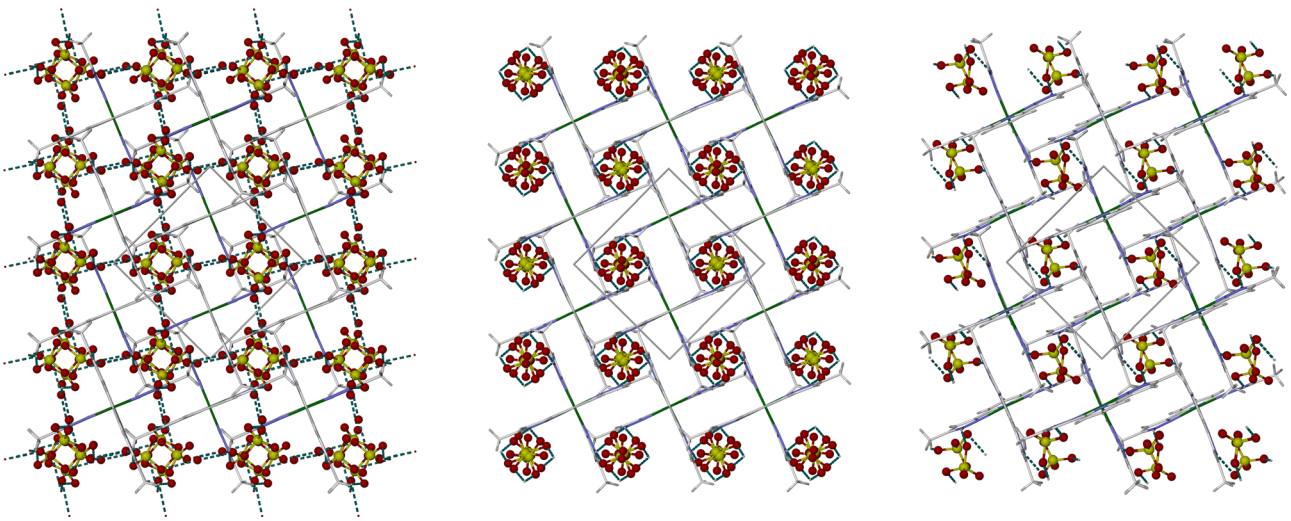

Fig. 1 Packing diagrams of **2b**·$2H_2O$ (left), phase B of **2b** (centre); and phase C (right), all viewed perpendicular to the (001) plane. Only one orientation of the disordered anions in the tetragonal phases is shown, but both components of the anion disorder about a C_2 axis in phase B are included. All atoms have arbitrary radii, with the complex cations de-emphasised for clarity.

Allowing for the different measurement temperatures, a is *ca.* 0.12 Å shorter and c is *ca.* 0.3 Å longer in phase B compared to the hydrated precursor phase (Table S1, ESI‡), leading to a small decrease in unit cell volume of *ca.* 22 Å^3 following dehydration. The disordered water half-molecule is no-longer apparent in phase B, with the ClO_4^- ion instead being more disordered to fill the space in the lattice (Fig. 1, centre). Since each anion is equally disordered between two hydrogen bond acceptor groups related by C_2 symmetry, on average each cation in phase B only forms two N–H···O hydrogen bonds. The reduced hydrogen bonding in phase B might contribute to lengthening of the distal Zn–N bonds from 2.179(3) Å in **2b**·2H_2O (at 120 K) to 2.226(3) Å in **2b** phase B (at 200 K).

The zinc cation structure is unchanged between 350–200 K. However, there is some evidence for reorientation of the disordered ClO_4^- ions on cooling between 300 and 250 K, which changes the hydrogen bond distribution in the crystal (Fig. S7, ESI‡). The symmetry-imposed anion disorder makes this hard to quantify, but displacement of the anions is an important step in the transformation to phase C described below.

The 200 K dataset of phase B has a high mosaicity, and gave larger refinement residuals than at the higher temperatures. Further cooling the same crystal to 120 K transformed it to a new phase C (triclinic, $P\bar{1}$, Z = 2). The crystal in phase C exhibited four-fold 90° rotational twinning in the (001) plane, but this was successfully resolved in the. *hkl* file allowing a full structure refinement. The asymmetric unit of phase C contains one cation and two anions, all on general crystallographic sites with no apparent disorder (Fig. 1, right).

The six-coordinate complex molecule in phase C is significantly distorted from the strict D_{2d} symmetry found in phase B (Fig. 2). That mostly reflects an acute *trans*-N{pyridine}–Fe–N{pyridine} angle (ϕ) from 180° in phase B to 168.09(9)° in phase C. This distortion positions each ClO_4^- ion in phase C to accept N–H···O hydrogen bonds from two different cations, thus doubling the number of hydrogen bonds in the lattice compared to phase B.

SCO in high-spin $[Fe(bpp)_2]^{2+}$ (bpp = 2,6-di{pyrazolyl}-pyridine) derivatives with reduced values of ϕ requires a significant change in coordination geometry, towards the less distorted geometry with $\phi \approx 180°$ preferred by the low-spin state.[53] That can lead to cooperative, hysteretic spin-transitions where SCO is observed.[36,54] However, it can also kinetically inhibit SCO in a material whose solid lattice is too rigid to accommodate that structure rearrangement.[55] Hence, $[Fe(bpp)_2]^{2+}$ complexes with $\phi \leq 172°$ are generally less likely to exhibit SCO below room temperature.[54] However, at 120–150 K ϕ in phase C of **2a** [167.62(7)°][22] and **2b** [168.09(9)°] differ by only 4σ, and are essentially equal crystallographically. Hence the molecular structure in phase C cannot, by itself, explain the inactivity of **1b** towards SCO.

Rather, the most significant crystallographic difference between the salts **2a** and **2b** is the temperature of the phase B → C transition. Phase C was observed at 285 K and below in single crystals of **2a**,[48] but was only achieved at 120 K in **2b**. The increased crystal mosaicity of phase B of **2b** at 200 K implies that measurement was close to the phase transition temperature. Be that as it may, the phase B → C transition temperature is at least 80–90 K lower in single crystals of the perchlorate salt.

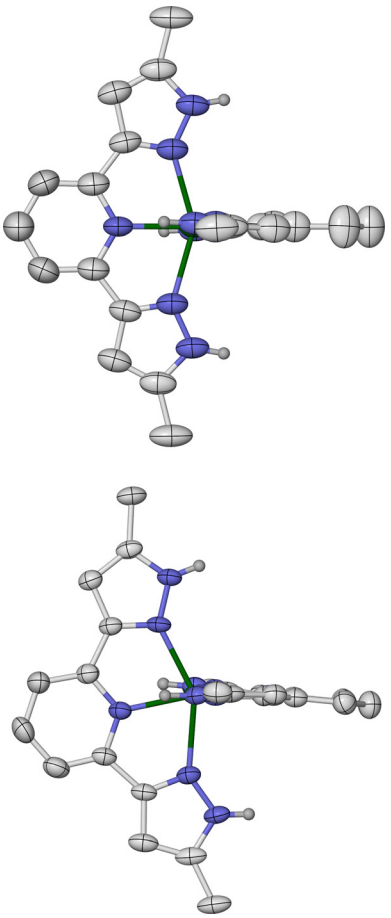

Fig. 2 The $[ZnL_2]^{2+}$ cations in **2b** phase B at 200 K (top), and phase C at 120 K (bottom), highlighting the smaller *trans*-N{pyridine}–Fe–N{pyridine} angle (ϕ) in phase C. Displacement ellipsoids are at the 50% probability level, and C-bound H atoms are omitted. Colour code: C, white; H, pale grey; Fe, green; N, blue.

The structural chemistry of **2b** was also probed by X-ray powder diffraction. That proved challenging, as inconsistent results were obtained from *in situ* dehydration of **2b**·2H_2O inside the sealed capillary sample holders used. Useful data were ultimately achieved from a sample inside an unsealed capillary, which allowed the moisture released by dehydration to escape. The data in Fig. 3 are a good match for crystallographic simulations from the different phases of the material (Fig. S11, ESI‡). There is also excellent agreement between these data and the different phases of **1b**,[47] confirming **2b** is a good structural model for the iron complex (Fig. 4).

Phase B was generated quantitatively *in situ* on heating the **2b**·2H_2O to 400 K. Interestingly, the phase B → C transformation does not happen abruptly under these conditions, but takes place over a 25 ± 5 K temperature range between 270 and 240 K. A small fraction of the sample does not transform to phase C below 240 K, and retains phase B at all temperatures. The same behaviour was shown by **1a**, **2a**[48] and **1b** (Fig. 4) in the

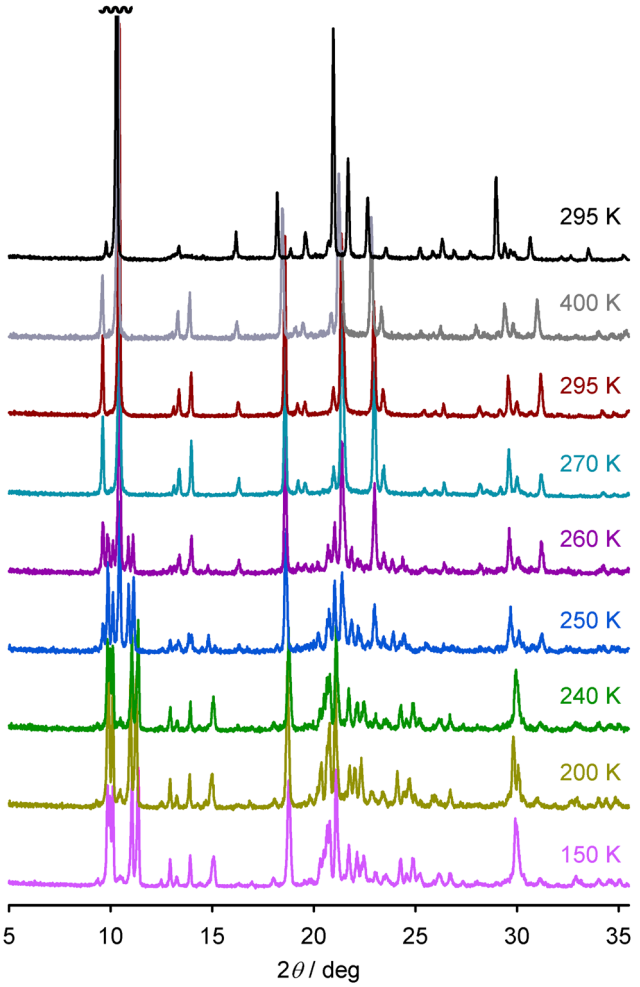

Fig. 3 Variable temperature X-ray powder diffraction data for **2b**·2H_2O. The sample was initially measured at 295 K; annealed at 400 K; then cooled sequentially from there to 150 K. The sample is a mixture of phases B and C at 260 and 250 K.

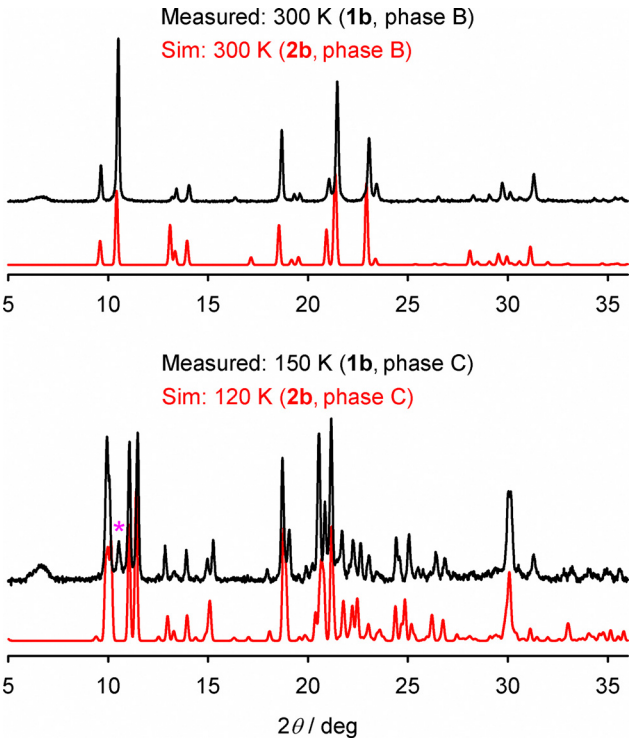

Fig. 4 Comparison of previously published powder diffraction data for the phases of **1b** (black), with simulations based on the crystal structures of **2b** (red). The starred peak in phase C implies a fraction of the sample remains in phase B on cooling.[48] Data for **1b** are taken from ref. 47.

powder diffractometer. Little change in the powder pattern of phase C was observed on cooling from 240 to 150 K. That is consistent with **1b**,[47] but contrasts with the BF_4^- salts **1a** and **2a** whose phase C structure is very temperature-dependent.[48] Evidently the structural plasticity in phase C of **1a** and **2a** is suppressed in the corresponding perchlorate salts.

A differential scanning calorimetry (DSC) measurement of **2b** showed a weak reversible endotherm attributable to the phase B → C transformation, centered at 268 K (Fig. S12, ESI‡). That is consistent with the onset of the transition on cooling in the powder diffraction measurement (Fig. 3). However, there is no evidence in the DSC data for the broadening of the phase transition observed by powder diffraction (Fig. 3). The different characteristics for the phase B → C transition in **2b** measured by crystallography, powder diffraction and DSC imply it depends on the measurement conditions and/or the history of the sample. That was not the case for **2a**, whose phase change was consistent within experimental error from same three measurement techniques.[48]

In a second experiment, the effect of replacing BF_4^- ions with ClO_4^- on the spin-transition in **1a** was probed using mixed-anion samples. Two compositions of $[FeL_2][BF_4]_z[ClO_4]_{2-z}\cdot 2H_2O$ (**1c**·2H_2O, z = 1.50; **1d**·2H_2O, z = 1.00) were isolated by co-crystallising preformed **1a** and **1b** in the appropriate ratios from undried nitromethane solution. The formulae of the products derived by C, H, N, Cl microanalysis were a good match for the expected compositions. Both the as-isolated materials were isomorphous with **1a**·2H_2O by powder diffraction (Fig. S13, ESI‡), and show the same dehydration behaviour on heating by TGA (Fig. S14, ESI‡).

As-isolated **1a**·2H_2O has a 1 : 1 high : low-spin population, but becomes fully high-spin around 350 K following *in situ* dehydration (Fig. 5, left; scan 1).[46] Anhydrous **1a** exhibits an abrupt spin-transition at $T_{1/2}$ = 205 K, with ΔT = 65 K hysteresis width on the initial scan (scan 2). The hysteresis narrows as the sample is aged by repeated thermal scanning (scans 3–6), eventually settling at $T_{1/2}$ = 208 K and ΔT = 37 K (Table 1). There are no further structural changes by powder diffraction during this process, so the hysteresis narrowing should simply reflect an increased number of defects and reduced crystal domain sizes in the aged material.[56–58]

The sample of **1c**·2H_2O behaves similarly (Fig. 5, centre), although its structural rearrangement after dehydration appears to occur more slowly than in the parent BF_4^- salt **1a**. That is evidenced by weak additional features in scans 2 and 3, which are not present in scans 4–6; and by the SCO hysteresis,

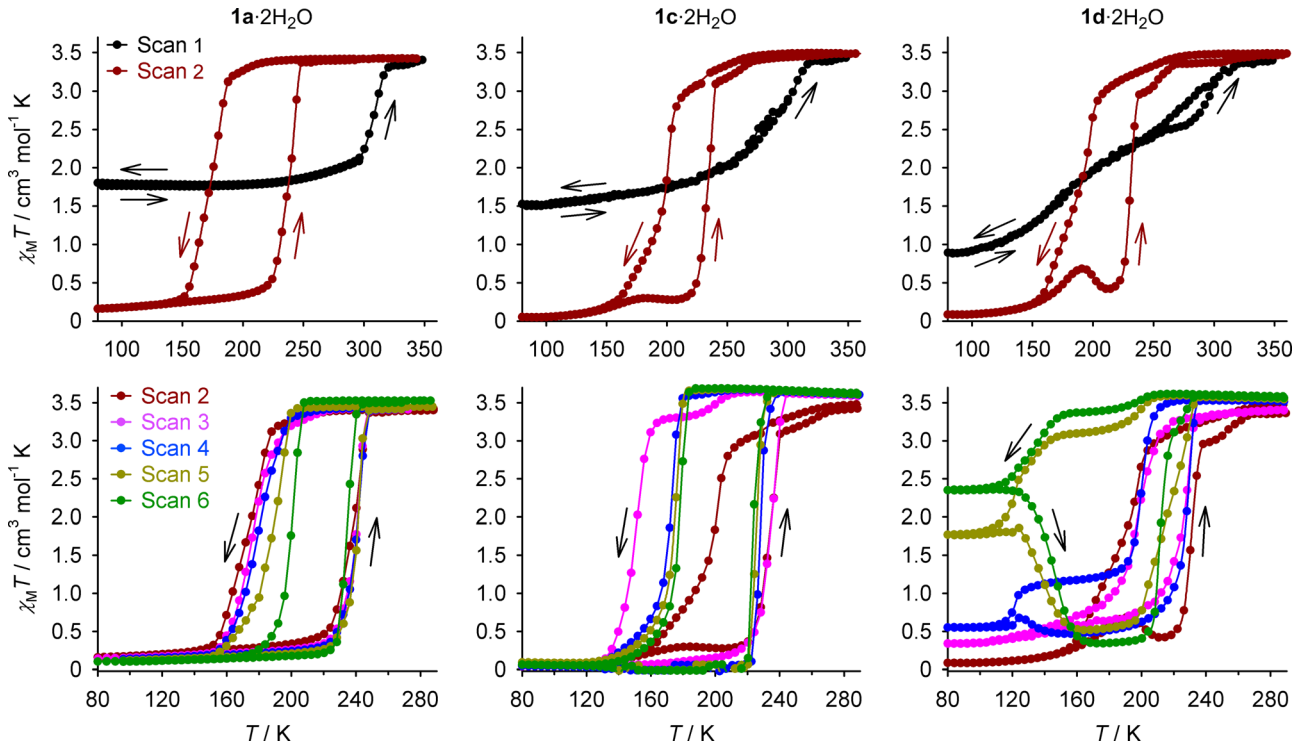

Fig. 5 Variable temperature magnetic data for **1a**·2H_2O (left), **1c**·2H_2O (centre); and **1d**·2H_2O (right), at scan rate 2 K min^{-1}. Top: An initial 290 → 5 → 350 K scan of the as-prepared samples showing their *in situ* dehydration (black), and the first 350 → 80 → 350 K scan of the dehydrated materials (red). Bottom: Repeated 350 → 80 → 350 K scans of the dehydrated compounds. The same colour coding is used for each material. The curves for **1c**·2H_2O and **1d**·2H_2O are shown individually in Fig. S15 and S16 (ESI‡), while the data for **1a**·2H_2O are replotted from ref. 46.

Table 1 Spin-transition temperatures for the anhydrous iron complex salts: in the initial scan following *in situ* annealing; the widest hysteresis loop obtained in the experiment; and, the final thermal scan (Fig. 5). Data were measured at scan rate 2 K min^{-1}, unless otherwise stated[59]

Sample	Experiment	$T_{1/2}\downarrow$/K	$T_{1/2}\uparrow$/K	$\Delta T_{1/2}$/K
1a[a]	1st scan	172	237	65
	Widest hysteresis	172	237	65
	Final hysteresis	190	227	37
1c	1st scan	199	233	34
	Widest hysteresis	149	234	85
	Final hysteresis	177	223	46
1d	1st scan	196	225	29
	Widest hysteresis[b]	145	223	78
	Final hysteresis[c]	—	—	—

[a] Data from ref. 46. [b] Taken from the 0.5 K min^{-1} scan in Fig. 6. [c] The final form of the hysteresis loop was not achieved for **1d**.

which widens substantially between scans 2 and 3 before contracting again in scans 4–6. The widest thermal hysteresis observed in this spin-transition is ΔT = 85 K (scan 3), which transforms to ΔT = 46 K at the end of the experiment (scan 6; Table 1). Hence, introducing 0.25 equiv. ClO_4^- into the lattice slightly lowers the temperature of the spin transition, but measurably increases its cooperativity.

Unlike **1a** and **1c**, freshly prepared **1d**·2H_2O shows a gradual but incomplete SCO on cooling (Fig. 5, right), with features resembling the structured SCO exhibited by the hydrated perchlorate salt (Fig. S1, ESI‡).[47] The first thermal scan following dehydration (scan 2) resembles **1c**, although the weak additional features on the main spin transition are more pronounced. The initial hysteretic spin-transition in scans 2–3 slowly transforms into a more cooperative transition during scans 4–6, which also becomes steadily less complete on the cooling branch of the hysteresis loop. That incompleteness reflects thermally induced excited spin state trapping (TIESST) of the sample at low temperature.[40,54,60–67] That is, kinetic trapping of a fraction of the sample in its high-spin state below *ca.* 120 K. The TIESST reflects that the cooling branch of the SCO hysteresis loop extends to a temperature where there is insufficient thermal energy in the lattice to facilitate the structural rearrangements associated with SCO.[66]

The kinetic nature of the effect is supported by the "reverse-SCO" feature on rewarming the sample above 120 K, where thermal relaxation of the material to its thermodynamic low-spin state can now take place.[67] Further warming to 210 K leads to an abrupt low → high-spin transition, which corresponds to the warming branch of the thermodynamic SCO thermal hysteresis loop. The TIESST in **1d** becomes progressively more efficient as the sample is cycled through scans 4–6. However, extra thermal cycles beyond scan 6 gave no significant additional changes, implying that represents the final form of the material (Fig. 5).

Notwithstanding the TIESST in **1d**, in other respects scan 3 of **1c**, and scans 5 and 6 of **1d**, closely resemble each other in

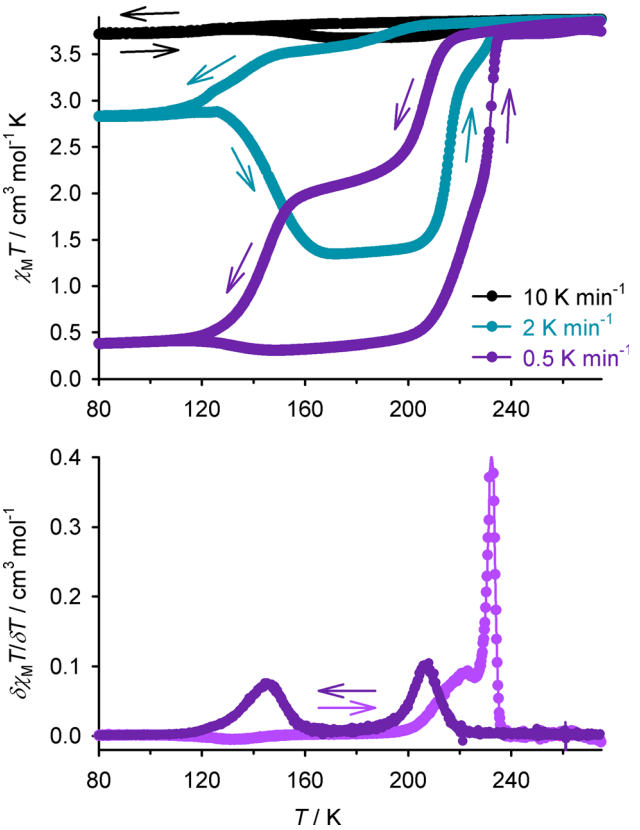

Fig. 6 Top: Variable temperature magnetic data from an aged sample of **1d** at different scan rates. Bottom: First derivative of the 0.5 K min^{-1} plot, showing the two distinct hysteretic features.

the 2 K min^{-1} measurements (Fig. 5). At those stages of the experiment, both materials show a wide hysteretic transition, preceded by a weaker high → low-spin step near 200 K on cooling which is not mirrored in the warming branch of the hysteresis loop. The 200 K feature may be a residual contribution from the initial, narrower hysteresis seen in scan 2, which occurs at the same temperature in cooling mode. Additional scanning of **1c** causes its evolution to a symmetrical spin-transition hysteresis loop, whereas **1d** remains trapped in that intermediate state under the same conditions.

The behaviour of an aged sample of **1d** was clarified by measurement at a slower scan rate of 0.5 K min^{-1}, where the kinetically slow high → low-spin transition proceeds to *ca.* 90% completeness (Fig. 6).[66–72] This revealed a structured spin-transition, occurring in two hysteretic steps of approximately equal height. Allowing for the different measurement conditions,[59] the narrow hysteresis component ($T_{1/2}\downarrow$ = 207, $T_{1/2}\uparrow$ = 232 K) resembles **1d** immediately following dehydration (Fig. 5, step 2), whereas the wider hysteresis step is similar to the wide hysteresis form of **1a** and **1c** (Table 1). Hence, as described above, the aged sample of **1d** appears to be a kinetically frozen mixture of intermediates in the transformation pathway towards its final, wide-hysteresis form.[73]

A sample of **1d**, dehydrated *in situ* on the powder diffractometer, adopts phase B at 353 K and phase C below room temperature (Fig. S17, ESI‡). The powder pattern of phase C in **1d** is not temperature-dependent, and has no obvious features to distinguish it from **1a** or **1b** under the same conditions.[46–48] The thermodynamic low-spin phase of **1d** was not achieved at 149 K, the lowest temperature achieved on that diffractometer. It is unclear how that how that correlates with the spin state properties of **1d** in its initial scans (Fig. 5).

Conclusions

Numerous studies have shown that salts of charged SCO complexes with different counterions often exhibit different spin-state behaviors.[1,2,19,74–79] When salts of the same complex are not isomorphous, such differences are a natural consequence of the different crystal packing in those materials, which are not then strictly comparable. Structure:function studies of isomorphous complex salts can be more informative however, as in this work.[45,65,80–84]

The zinc(II) complex **2b** has proven to be a useful structural model for its iron(II) analogue **1b** (Fig. 4). While **2b**·2H$_2$O and **2b** are isomorphous with previously reported **2a**·2H$_2$O and **2a**,[48] the analysis of **2b** leads to two useful observations. First, although the complex in phase C of **2b** deviates significantly from an ideal octahedral geometry (Fig. 2), the degree of distortion at 120 K is almost identical to **2a** around the same temperature. Powder diffraction shows the structures of high-spin **1b** (Fig. 4) and SCO-active **1a**[48] closely match the zinc complexes under these conditions. Hence, although such distortions can be responsible for inhibition of SCO in complexes related to $[FeL_2]^{2+}$,[54,55] the different spin state behaviours of **1a** and **1b** are not a reflection of their molecular structure.

The phase B → C transition in **2b** also occurs sluggishly, and appears to depend on the measurement conditions or sample history. It was observed over a 25 ± 5 K temperature window on cooling between 270–240 K by powder diffraction (Fig. 3), but was only achieved below 200 K on the single crystal diffractometer. That contrasts with **2a**, where the same transformation occurs abruptly at 290–295 K by both techniques.[48] The inconsistent behavior shown by **2b** suggests the structural rearrangement associated with the phase transition may have a higher kinetic barrier than in the BF_4^- salt **2a**.

The BF_4^- salt **1a**·2H$_2$O transforms cleanly upon dehydration to phase C, which initially exhibits a wide, symmetric spin-transition hysteresis [form (ii); Scheme 2] which slowly narrows on repeated scanning [form (iii)].[46] Magnetic measurements on

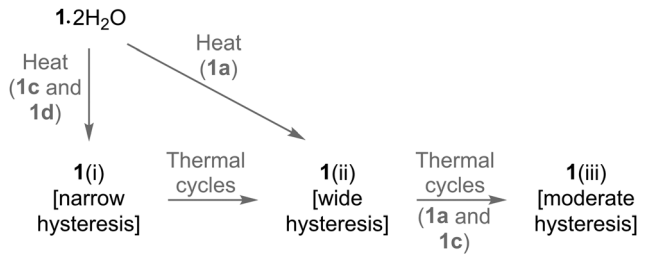

Scheme 2 The different stages in the transformation of **1a**, **1c** and **1d** after dehydration, as distinguished by their spin-transition thermal hysteresis.

the mixed-anion salts $[FeL_2][BF_4]_z[ClO_4]_{2-z}\cdot 2H_2O$ (**1c**·$2H_2O$ and **1d**·$2H_2O$) follow the same sequence but more slowly, and reveal a new intermediate state along that pathway. Freshly dehydrated **1c** and **1d** (scan 2, Fig. 5) show an initial SCO hysteresis width $\Delta T_{1/2}$ *ca.* 30 K at 2 K min^{-1} [form (i)] which was not observed for **1a**. Further scanning converts this species to form (ii), with $\Delta T_{1/2} \geq 80$ K. Forms (i) and (ii) are observed together in scan 3 of **1c**, and scans 4–6 of **1d** (Fig. 5). Form (iii) was ultimately achieved for **1c** by additional thermal scans, but **1d** remains trapped as a static mixture of forms (i) and (ii) after *ca.* 5 thermal cycles. Conversion of **1d** to form (iii) was not observed in this study.

The slower kinetics of the structure transformations in **1d** are also evident in the thermal trapping of the high-spin state (TIESST) of form (ii) below 120 K (Fig. 6). That is not exhibited by **1c** form (ii), even though its spin-transition occurs at similar temperatures to **1d** at a 2 K min^{-1} scan rate (Fig. 5). Hence, while **1c** and **1d** have similar spin state energetics, the internal dynamics of **1d** must be intrinsically slower than in **1c**, to inhibit its SCO.

Forms (ii) and (iii) of **1a** are isomorphous by powder diffraction, and undergo the same sequence of phase B {high-spin} → C {high-spin} → E {low-spin} phase transitions on cooling.[48] Therefore the smaller hysteresis loop in form (iii) was attributed to it possessing smaller crystal domains or more microstructural defects, following multiple cycling through its various phase changes.[56–58]

While more limited characterisation of **1d** by powder diffraction is available, we found no evidence for additional crystal phases in **1d** above 150 K, beyond the same phases B and C shown by the other materials (Fig. S17, ESI‡). Hence, on this evidence, the form (i) → (ii) → (iii) process (Scheme 2) simply involves a slow annealing of the samples upon repeated cycling across the phase B → C → E → C → B phase transitions.[48] While the structure of phase E is still unknown, the phase B → C transition involves both a deformation of the complex, and a substantial rearrangement of the anions in the lattice (Fig. 1 and 2). That rearrangement occurs more slowly for **2b** than in **2a**, implying the larger ClO_4^- ions in **2b** impede that structural reorganisation.

Taken together, the data in this study imply the structural evolution of $[FeL_2][BF_4]_z[ClO_4]_{2-z}$ (**1a–1d**) following dehydration becomes progressively slower as the fraction of perchlorate ions increases, in the order **1a** ($z = 2$) > **1c** ($z = 1.5$) > **1d** ($z = 1$) > **1b** ($z = 0$). The same pattern of crystal phases is observed in **1a**, **1b** and **1d** within the relevant temperature range; and, the molecular structures of **1a** and **1b** near the spin-transition temperature are essentially the same. While the materials are extensively hydrogen-bonded, that should not contribute significantly to these differences since BF_4^- and ClO_4^- are comparably weak hydrogen bond acceptors.[85] Rather, we propose the slower structural rearrangements in the presence of ClO_4^- reflect its larger size, which impedes its reorientation as the phase changes are cycled.[86]

We conclude the high-spin nature of **1b** reflects its slower lattice dynamics compared with isomorphous, SCO-active **1a**, in the presence of ClO_4^- ions. Effectively, the partial TIESST shown by **1d** below 120 K at moderate scan rates (Fig. 5 and 6) becomes complete in **1b**, so its SCO is kinetically inhibited.[66]

Experimental

2,6-Bis(5-methyl-1*H*-pyrazol-3-yl)pyridine (L),[87] $[FeL_2][BF_4]_2\cdot 2H_2O$ (**1a**·$2H_2O$)[46] and $[FeL_2][ClO_4]_2\cdot 2H_2O$ (**1b**·$2H_2O$)[47] were prepared by the literature procedures.

Synthesis of $[ZnL_2][ClO_4]_2\cdot 2H_2O$ (2b·$2H_2O$)

A solution of L (0.5 g, 2.1 mmol) and $Zn[ClO_4]_2\cdot 4H_2O$ (0.41 g, 1.1 mmol) in MeOH (50 cm^3) was stirred until all the solid had dissolved. The colourless solution was filtered, and concentrated to *ca.* 5 cm^3. Addition of excess diethyl ether afforded the complex as a white precipitate. The crude material was recrystallised from undried nitromethane by slow diffusion of diethyl ether vapour, which yielded pale yellow dihydrate crystals suitable for X-ray analysis. Yield 0.58 g, 68%. Found: C, 40.4; H, 3.58; N, 17.9%. Calcd for $C_{26}H_{26}Cl_2N_{10}O_8Zn\cdot 2H_2O$ C, 40.1; H, 3.88; N, 18.0%.

Synthesis of $[FeL_2][BF_4]_z[ClO_4]_{2-z}\cdot 2H_2O$ (1c·$2H_2O$; $z \approx 1.50$)

A mixture of **1a**·$2H_2O$ (0.10 g, 1.4 mmol) and **1b**·$2H_2O$ (0.034 g, 0.14 mmol) was dissolved in hot water. After all the solid had dissolved the solution was filtered hot, then cooled slowly to room temperature over a period of 24 h. The product was a brown microcrystalline solid. Yield 0.12 g, 90%. Found: C, 41.8; H, 3.95; N, 18.5; Cl, 2.30%. Calcd for $C_{26}H_{26}B_{1.50}Cl_{0.50}F_6FeN_{10}O_2\cdot 2H_2O$ C, 41.6; H, 4.03; N, 18.7; Cl, 2.36%.

Synthesis of $[FeL_2][BF_4]_z[ClO_4]_{2-z}\cdot 2H_2O$ (1d·$2H_2O$; $z \approx 1.00$)

Method as for **1c**·$2H_2O$, using **1a**·$2H_2O$ (0.068 g, 0.095 mmol) and **1b**·$2H_2O$ (0.070 g, 0.095 mmol). Yield 0.13 g, 94%. Found: C, 41.4; H, 3.90; N, 18.6; Cl, 4.60%. Calcd for $C_{26}H_{26}BClF_4FeN_{10}O_4\cdot 2H_2O$ C, 41.3; H, 4.00; N, 18.5; Cl, 4.69%.

Caution

Although we have experienced no problems when using the perchlorate salts in this work, metal–organic perchlorates are potentially explosive and should be handled with care in small quantities.

Single crystal structure analyses

All diffraction data for **2b**·$2H_2O$ and **2b** were measured from the same crystal, with an Agilent Supernova dual-source diffractometer using monochromated Cu-K_α (λ = 1.5418 Å) radiation. The diffractometer was fitted with an Oxford Cryostream low-temperature device. The structures were solved by direct methods (SHELXS[88]), and developed by full least-squares refinement on F^2 (SHELXL-2018[88]). Crystallographic figures were generated using XSEED,[89] while other publication materials were prepared with OLEX2.[90] Experimental details for the structure are listed in Table S1 (ESI‡), while details of the crystallographic refinements are also given in the ESI.‡

Other measurements

Elemental microanalyses were performed by the microanalytical service at the University of Leeds School of Chemistry, or London Metropolitan University School of Human Sciences. Thermogravimetric analyses employed a TA Instruments TGA Q50 analyser with a temperature ramp of 10 K min^{-1} under a stream of nitrogen gas, while differential scanning calorimetry measurements used a TA Instruments DSC Q20 calorimeter, also with a temperature ramp of 10 K min^{-1}. X-Ray powder diffraction data for **2b** were obtained using a Bruker D8-A25 diffractometer in transmission capillary geometry, with a Ge(111) Johanssen monochromator and a Lynxeye detector. The diffractometer was fitted with an Oxford Cryostream low-temperature device. Other powder diffraction measurements employed a Bruker D8 Advance A25 diffractometer. Both diffractometers employed Cu-$K_{\alpha 1}$ radiation (λ = 1.5406 Å). Magnetic susceptibility measurements were performed on a Quantum Design MPMS SQUID magnetometer, in an applied field of 5000 G. A temperature ramp of 2 K min^{-1} was used for these measurements, unless otherwise stated. A diamagnetic correction for the sample was estimated from Pascal's constants,[91] and a previously measured diamagnetic correction for the sample holder, were applied to the data.

Conflicts of interest

There are no conflicts to declare.

Acknowledgements

The authors thank Drs Tim Comyn (University of Leeds) and Laurence Kershaw Cook (University of Leeds, now University of Liverpool) for help with measurements on **1c** and **1d**. This work was funded by the University of Leeds (Brotherton Scholarship to TDR) and the EPSRC (DTP studentship to TDR). The powder diffraction facility at the University of Oslo is supported by the Norwegian national infrastructure for X-ray diffraction and scattering (RECX), and by the Research Council of Norway *via* the TomoCAT researcher project (no. 301619).

Notes and references

1 *Spin Crossover in Transition Metal Compounds I–III: Topics in Current Chemistry*, ed. P. Gütlich and H. A. Goodwin, Springer, New York, 2004, vol. 233–235.
2 *Spin-crossover materials – properties and applications*, ed. M. A. Halcrow, John Wiley & Sons, Chichester, UK, 2013, p. 568.
3 J. Zarembowitch, F. Varret, A. Hauser, J. A. Real and K. Boukheddaden, *C. R. Chim.*, 2018, **21**, 1056–1059.
4 Z.-S. Yao, Z. Tang and J. Tao, *Chem. Commun.*, 2020, **56**, 2071–2086.
5 K. Senthil Kumar and M. Ruben, *Coord. Chem. Rev.*, 2017, **346**, 176–205.
6 S. Hayami, S. M. Holmes and M. A. Halcrow, *J. Mater. Chem. C*, 2015, **3**, 7775–7778.
7 A. Enriquez-Cabrera, A. Rapakousiou, M. Piedrahita Bello, G. Molnár, L. Salmon and A. Bousseksou, *Coord. Chem. Rev.*, 2020, **419**, 213396.
8 M. Wang, Z.-Y. Li, R. Ishikawa and M. Yamashita, *Coord. Chem. Rev.*, 2021, **435**, 213819.
9 Y. Sekine, R. Akiyoshi and S. Hayami, *Coord. Chem. Rev.*, 2022, **469**, 214663.
10 O. I. Kucheriv, V. V. Oliynyk, V. V. Zagorodnii, V. L. Launets and I. A. Gural'skiy, *Sci. Rep.*, 2016, **6**, 38334.
11 M. D. Manrique-Juárez, F. Mathieu, A. Laborde, S. Rat, V. Shalabaeva, P. Demont, O. Thomas, L. Salmon, T. Leichle, L. Nicu, G. Molnár and A. Bousseksou, *Adv. Funct. Mater.*, 2018, **28**, 1801970.
12 V. Nagy, I. Suleimanov, G. Molnár, L. Salmon, A. Bousseksou and L. Csóka, *J. Mater. Chem. C*, 2015, **3**, 7897–7905.
13 M. Piedrahita-Bello, J. E. Angulo-Cervera, R. Courson, G. Molnár, L. Malaquin, C. Thibault, B. Tondu, L. Salmon and A. Bousseksou, *J. Mater. Chem. C*, 2020, **8**, 6001–6005.
14 M. S. Reis, *Coord. Chem. Rev.*, 2020, **417**, 213357.
15 K. Ridier, Y. Zhang, M. Piedrahita-Bello, C. M. Quintero, L. Salmon, G. Molnár, C. Bergaud and A. Bousseksou, *Adv. Mater.*, 2020, **32**, 2000987.
16 K. Senthil Kumar and M. Ruben, *Angew. Chem., Int. Ed.*, 2021, **60**, 7502–7521.
17 L. Kipgen, M. Bernien, F. Tuczek and W. Kuch, *Adv. Mater.*, 2021, **33**, 2008141 and 2021, 33, 2170354 (correction).
18 E. Coronado, *Nat. Rev. Mater.*, 2020, **5**, 87–104.
19 M. A. Halcrow, *Chem. Soc. Rev.*, 2011, **40**, 4119–4142.
20 P. Guionneau, M. Marchivie and G. Chastanet, *Chem. – Eur. J.*, 2021, **27**, 1483–1486.
21 M. A. Halcrow, I. Capel Berdiell, C. M. Pask and R. Kulmaczewski, *Inorg. Chem.*, 2019, **58**, 9811–9821.
22 H. Fourati, M. Ndiaye, M. Sy, S. Triki, G. Chastanet, S. Pillet and K. Boukheddaden, *Phys. Rev. B*, 2022, **105**, 174436 and references therein.
23 M. Chergui and E. Collet, *Chem. Rev.*, 2017, **117**, 11025–11065.
24 K. J. Gaffney, *Chem. Sci.*, 2021, **12**, 8010–8025.
25 M. A. Halcrow, *Chem. Lett.*, 2014, **43**, 1178–1188.
26 O. Kahn and C. Jay Martinez, *Science*, 1998, **279**, 44–48.
27 J.-F. Létard, P. Guionneau and L. Goux-Capes, *Top. Curr. Chem.*, 2004, **235**, 221–249.
28 J.-F. Létard, P. Guionneau, E. Codjovi, O. Lavastre, G. Bravic, D. Chasseau and O. Kahn, *J. Am. Chem. Soc.*, 1997, **119**, 10861–10862.
29 S. Dorbes, L. Valade, J. A. Real and C. Faulman, *Chem. Commun.*, 2005, 69–71.
30 G. A. Craig, J. S. Costa, O. Roubeau, S. J. Teat and G. Aromí, *Chem. – Eur. J.*, 2011, **17**, 3120–3127.
31 S. Kang, Y. Shiota, A. Kariyazaki, S. Kanegawa, K. Yoshisawa and O. Sato, *Chem. – Eur. J.*, 2016, **22**, 532–538.
32 A. Djemel, O. Stefanczyk, M. Marchivie, E. Trzop, E. Collet, C. Desplanches, R. Delimi and G. Chastanet, *Chem. – Eur. J.*, 2018, **24**, 14760–14767.
33 M. Grzywa, R. Röß-Ohlenroth, C. Muschielok, H. Oberhofer, A. Błachowski, J. Żukrowski, D. Vieweg, H.-A. Krug von Nidda and D. Volkmer, *Inorg. Chem.*, 2020, **59**, 10501–10511.

34 A. Benchohra, Y. Li, L.-M. Chamoreau, B. Baptiste, E. Elkaïm, N. Guillou, D. Kreher and R. Lescouëzec, *Angew. Chem., Int. Ed.*, 2021, **60**, 8803–8807.
35 M. Seredyuk, K. Znovjyak, F. J. Valverde-Muñoz, I. da Silva, M. C. Muñoz, Y. S. Moroz and J. A. Real, *J. Am. Chem. Soc.*, 2022, **144**, 14297–14309.
36 N. Suryadevara, A. Mizuno, L. Spieker, S. Salamon, S. Sleziona, A. Maas, E. Pollmann, B. Heinrich, M. Schleberger, H. Wende, S. K. Kuppusamy and M. Ruben, *Chem. – Eur. J.*, 2022, **28**, e202103853.
37 D. L. Reger, J. D. Elgin, M. D. Smith, F. Grandjean, L. Rebbouh and G. J. Long, *Eur. J. Inorg. Chem.*, 2004, 3345–3352.
38 B. Weber, W. Bauer and J. Obel, *Angew. Chem., Int. Ed.*, 2008, **47**, 10098–10101.
39 H. J. Shepherd, T. Palamarciuc, P. Rosa, P. Guionneau, G. Molnár, J.-F. Létard and A. Bousseksou, *Angew. Chem., Int. Ed.*, 2012, **51**, 3910–3914.
40 V. Gómez, C. Sáenz de Pipaón, P. Maldonado-Illescas, J. C. Waerenborgh, E. Martin, J. Benet-Buchholz and J. R. Galán-Mascarós, *J. Am. Chem. Soc.*, 2015, **137**, 11924–11927.
41 E. König, G. Ritter, S. K. Kulshreshtha and N. Csatary, *Inorg. Chem.*, 1984, **23**, 1903–1910.
42 T. Buchen, P. Gütlich, K. H. Sugiyarto and H. A. Goodwin, *Chem. – Eur. J.*, 1996, **2**, 1134–1138.
43 S. Hayami, Z.-Z. Gu, H. Yoshiki, A. Fujishima and O. Sato, *J. Am. Chem. Soc.*, 2001, **123**, 11644–11650.
44 M. B. Bushuev, V. A. Daletsky, D. P. Pishchur, Y. V. Gatilov, I. V. Korolkov, E. B. Nikolaenkova and V. P. Krivopalov, *Dalton Trans.*, 2014, **43**, 3906–3910.
45 W. Phonsri, P. Harding, L. Liu, S. G. Telfer, K. S. Murray, B. Moubaraki, T. M. Ross, G. N. L. Jameson and D. J. Harding, *Chem. Sci.*, 2017, **8**, 3949–3959.
46 T. D. Roberts, F. Tuna, T. L. Malkin, C. A. Kilner and M. A. Halcrow, *Chem. Sci.*, 2012, **3**, 349–354.
47 T. D. Roberts, M. A. Little, F. Tuna, C. A. Kilner and M. A. Halcrow, *Chem. Commun.*, 2013, **49**, 6280–6282.
48 C. M. Pask, S. Greatorex, R. Kulmaczewski, A. Baldansuren, E. J. L. McInnes, F. Bamiduro, M. Yamada, N. Yoshinari, T. Konno and M. A. Halcrow, *Chem. – Eur. J.*, 2020, **26**, 4833–4841. The 'B', 'C' and 'E' labels for the crystal phases of the anhydrous materials used in ref. 48, and in this work, were chosen to be consistent with ref. 46.
49 C. Carbonera, C. A. Kilner, J.-F. Létard and M. A. Halcrow, *Dalton Trans.*, 2007, 1284–1292.
50 H. Dote, M. Kaneko, K. Inoue and S. Nakashima, *Bull. Chem. Soc. Jpn.*, 2018, **91**, 71–81.
51 I. Capel Berdiell, R. Kulmaczewski, N. Shahid, O. Cespedes and M. A. Halcrow, *Chem. Commun.*, 2021, **57**, 6566–6569.
52 I. Dance and M. Scudder, *CrystEngComm*, 2009, **11**, 2233–2247.
53 L. J. Kershaw Cook, R. Mohammed, G. Sherborne, T. D. Roberts, S. Alvarez and M. A. Halcrow, *Coord. Chem. Rev.*, 2015, **289–290**, 2–12.
54 L. J. Kershaw Cook, F. L. Thorp-Greenwood, T. P. Comyn, O. Cespedes, G. Chastanet and M. A. Halcrow, *Inorg. Chem.*, 2015, **54**, 6319–6330.
55 S. Vela, J. J. Novoa and J. Ribas-Arino, *Phys. Chem. Chem. Phys.*, 2014, **16**, 27012–27024.
56 Y. Miyazaki, T. Nakamoto, S. Ikeuchi, K. Saito, A. Inaba, M. Sorai, T. Tojo, T. Atake, G. S. Matouzenko, S. Zein and S. A. Borshch, *J. Phys. Chem. B*, 2007, **111**, 12508–12517.
57 M. B. Bushuev, D. P. Pishchur, V. A. Logvinenko, Y. V. Gatilov, I. V. Korolkov, I. K. Shundrina, E. B. Nikolaenkova and V. P. Krivopalov, *Dalton Trans.*, 2016, **45**, 107–120.
58 A. Grosjean, N. Daro, S. Pechev, C. Etrillard, G. Chastanet and P. Guionneau, *Eur. J. Inorg. Chem.*, 2018, 429–434.
59 Hysteresis width in SCO transitions can be scan-rate dependent. Hysteresis generally increases with faster temperature scanning, with the cooling branch of the hysteresis loop being more affected by scan rate than the warming branch. A slower scan rate was required to reveal the features of the SCO hysteresis in anhydrous **1d** (0.5 K min^{-1}; Fig. 6), compared to **1a** and **1c** (2 K min^{-1}; Fig. 5). Hence, $T_{1/2}$ values quoted for anhydrous **1d** in Table 1 and the text will be intrinsically some degrees higher, and $\Delta T_{1/2}$ narrower, than if they had been measured under the same conditions as **1a** and **1c**. S. Brooker, *Chem. Soc. Rev.*, 2015, **44**, 2880–2892.
60 M. Marchivie, P. Guionneau, J.-F. Létard, D. Chasseau and J. A. K. Howard, *J. Phys. Chem. Solids*, 2004, **65**, 17–23.
61 G. A. Craig, J. S. Costa, S. J. Teat, O. Roubeau, D. S. Yufit, J. A. K. Howard and G. Aromí, *Inorg. Chem.*, 2013, **52**, 7203–7209.
62 K. D. Murnaghan, C. Carbonera, L. Toupet, M. Griffin, M. M. Dîrtu, C. Desplanches, Y. Garcia, E. Collet, J.-F. Létard and G. G. Morgan, *Chem. – Eur. J.*, 2014, **20**, 5613–5618.
63 J. Weihermüller, S. Schlamp, B. Dittrich and B. Weber, *Inorg. Chem.*, 2019, **58**, 1278–1289.
64 T. Boonprab, S. J. Lee, S. G. Telfer, K. S. Murray, W. Phonsri, G. Chastanet, E. Collet, E. Trzop, G. N. L. Jameson, P. Harding and D. J. Harding, *Angew. Chem., Int. Ed.*, 2019, **58**, 11811–11815.
65 R. Kulmaczewski, E. Trzop, L. J. Kershaw Cook, E. Collet, G. Chastanet and M. A. Halcrow, *Chem. Commun.*, 2017, **53**, 13268–13271.
66 Y. S. Ye, X. Q. Chen, Y. D. Cai, B. Fei, P. Dechambenoit, M. Rouzières, C. Mathonière, R. Clérac and X. Bao, *Angew. Chem., Int. Ed.*, 2019, **58**, 18888–18891.
67 N. Paradis, G. Chastanet, T. Palamarciuc, P. Rosa, V. Varret, K. Boukheddaden and J.-F. Létard, *J. Phys. Chem. C*, 2015, **119**, 20039–20050.
68 V. A. Money, C. Carbonera, J. Elhaïk, M. A. Halcrow, J. A. K. Howard and J.-F. Létard, *Chem. – Eur. J.*, 2007, **13**, 5503–5514.
69 J.-F. Létard, S. Asthana, H. J. Shepherd, P. Guionneau, A. E. Goeta, N. Suemura, R. Ishikawa and S. Kaizaki, *Chem. – Eur. J.*, 2012, **18**, 5924–5934.
70 E. Milin, V. Patinec, S. Triki, E. Bendeif, S. Pillet, M. Marchivie, G. Chastanet and K. Boukheddaden, *Inorg. Chem.*, 2016, **55**, 11652–11661.
71 Y.-C. Chen, Y. Meng, Y.-J. Dong, X.-W. Song, G.-Z. Huang, C.-L. Zhang, Z.-P. Ni, J. Navařík, O. Malina, R. Zbořil and M.-L. Tong, *Chem. Sci.*, 2020, **11**, 3281–3289.

72 V. Jornet-Mollá, C. Giménez-Saiz, L. Cañadillas-Delgado, D. S. Yufit, J. A. K. Howard and F. M. Romero, *Chem. Sci.*, 2021, **12**, 1038–1053.
73 The two steps might also reflect a transformation to a new phase of the material, containing two unique iron environments that undergo SCO independently.[92–96] However, for the reasons described in the text, the data are more consistent with the aged sample being a kinetically frozen intermediate form of the phase transformation of **1d**.
74 P. Gütlich, A. Hauser and H. Spiering, *Angew. Chem., Int. Ed Engl.*, 1994, **33**, 2024–2054.
75 M. A. Halcrow, *Polyhedron*, 2007, **26**, 3523–3576.
76 M. A. Halcrow, *Coord. Chem. Rev.*, 2009, **253**, 2493–2514.
77 G. A. Craig, O. Roubeau and G. Aromí, *Coord. Chem. Rev.*, 2014, **269**, 13–31.
78 D. J. Harding, P. Harding and W. Phonsri, *Coord. Chem. Rev.*, 2016, **313**, 38–61.
79 K. Senthil Kumar, Y. Bayeh, T. Gebretsadik, E. Elemo, M. Gebrezgiabher, M. Thomas and M. Ruben, *Dalton Trans.*, 2019, **48**, 15321–15337.
80 M. Hostettler, K. W. Törnroos, D. Chernyshov, B. Vangdal and H.-B. Bürgi, *Angew. Chem., Int. Ed.*, 2004, **43**, 4589–4594.
81 M. Yamada, H. Hagiwara, H. Torigoe, N. Matsumoto, M. Kojima, F. Dahan, J.-P. Tuchagues, N. Re and S. Iijima, *Chem. – Eur. J.*, 2006, **12**, 4536–4549.
82 T. Sato, K. Nishi, S. Iijima, M. Kojima and N. Matsumoto, *Inorg. Chem.*, 2009, **48**, 7211–7229.
83 M. A. Al-Azzani, F. Al-Mjeni, R. Mitsuhashi, M. Mikuriya, I. A. Al-Omari, C. C. Robertson, E. Bill and M. S. Shongwe, *Chem. – Eur. J.*, 2020, **26**, 4766–4779.
84 R. Díaz-Torres, W. Phonsri, K. S. Murray, L. Liu, M. Ahmed, S. M. Neville, P. Harding and D. J. Harding, *Inorg. Chem.*, 2020, **59**, 13784–13791.
85 N. Galland, C. Laurence and J.-Y. Le Questel, *J. Org. Chem.*, 2022, **87**, 7264–7273.
86 The volume of a ClO_4^- ion (47 Å^3) is 24% larger than for a BF_4^- ion (38 Å^3). D. M. P. Mingos and A. L. Rohl, *J. Chem. Soc., Dalton Trans.*, 1991, 3419–3425.
87 Y. Zhou, W. Chen and D. Wang, *Dalton Trans.*, 2008, 1444–1453.
88 G. M. Sheldrick, *Acta Crystallogr. Sect. C*, 2015, **71**, 3–8.
89 L. J. Barbour, *J. Appl. Crystallogr.*, 2020, **53**, 1141–1146.
90 O. V. Dolomanov, L. J. Bourhis, R. J. Gildea, J. A. K. Howard and H. Puschmann, *J. Appl. Crystallogr.*, 2009, **42**, 339–341.
91 C. J. O'Connor, *Prog. Inorg. Chem.*, 1982, **29**, 203–283.
92 M. S. Shongwe, B. A. Al-Rashdi, H. Adams, M. J. Morris, M. Mikuriya and G. R. Hearne, *Inorg. Chem.*, 2007, **46**, 9558–9568.
93 J. Tang, J. S. Costa, S. Smulders, G. Molnár, A. Bousseksou, S. J. Teat, Y. Li, G. A. van Albada, P. Gamez and J. Reedijk, *Inorg. Chem.*, 2009, **48**, 2128–2135.
94 Y.-Y. Zhu, H.-Q. Li, Z.-Y. Ding, X.-J. Lü, L. Zhao, Y.-S. Meng, T. Liu and S. Gao, *Inorg. Chem. Front.*, 2016, **3**, 1624–1636.
95 S. Chorazy, T. Charytanowicz, D. Pinkowicz, J. Wang, K. Nakabayashi, S. Klimke, F. Renz, S. Ohkoshi and B. Sieklucka, *Angew. Chem., Int. Ed.*, 2020, **59**, 15741–15749.
96 O. I. Kucheriv, S. I. Shylin, V. Y. Sirenko, V. Ksenofontov, W. Tremel, I.-A. Dascălu, S. Shova and I. A. Gural'skiy, *Chem. – Eur. J.*, 2022, **28**, e202200924.

